Constant Stress and Pressure Rheology of Colloidal Suspensions

Mu Wang[*] and John F. Brady[†]

Division of Chemistry and Chemical Engineering, California Institute of Technology, Pasadena, California 91125, USA

We study the constant stress and pressure rheology of dense hard-sphere colloidal suspensions using Brownian dynamics simulation. Expressing the flow behavior in terms of the friction coefficient—the ratio of shear to normal stress—reveals a shear arrest point from the collapse of the rheological data in the non-Brownian limit. The flow curves agree quantitatively (when scaled) with the experiments of Boyer *et al.* [Phys. Rev. Lett. 107, 188301 (2011)]. Near suspension arrest, both the shear and the incremental normal viscosities display a universal power law divergence. This work shows the important role of jamming on the arrest of colloidal suspensions and illustrates the care needed when conducting and analyzing experiments and simulations near the flow-arrest transition.

Amorphous materials such as metallic glasses, granular matter, and colloidal suspensions exhibit a range of flow behaviors including shear thickening [1], particle migration [2], shear banding [3], etc. The most fundamental and universal aspect of their rheology is a flow-arrest transition that takes place at either increased density or reduced temperature and is summarized by various "jamming diagrams," pioneered by Liu and Nagel [4–6]. Extensive computational and experimental investigations reveal that the flow-arrest transition is affected by the interplay among thermal fluctuations [6–10] and particle geometry and interactions [11–14]. Distinct behaviors have been observed for strong and weak thermal fluctuations, but the connection between the two limits is an open question.

In this Letter we present a unified perspective on the flow-arrest transition spanning the entire range between the thermal and athermal limits. For simplicity, our study focuses on hard-sphere colloidal dispersions. Experiments and simulations at fixed volume (fraction) have found the suspension viscosity to diverge algebraically at a critical volume fraction: $\eta_s \propto (\phi_c - \phi)^{-\delta}$, where ϕ is the volume fraction and δ is the exponent. With strong thermal fluctuations the colloidal glass transition is observed: $\phi_c \approx$ 0.58–0.60 and $\delta \approx 2.2$–2.6 [7,15–17]. In the limit of the jamming transition where thermal fluctuations are weak, $\phi_c \approx 0.585$–0.64 and $\delta \approx 2.0$ [9,18,19]. Moreover, ϕ_c is sensitive to the particle size polydispersity [20], particle surface asperity [5], and even the sample preparation protocol [21]. Traditionally, the different exponents are interpreted as signatures of distinct physical processes—the colloidal glass vs the jamming transition [9]. Here we show that when the suspension pressure, instead of the volume, is held fixed under shear, a universal exponent and behavior emerges.

A challenge to dense suspension rheology is the divergence of properties such as viscosity and yield stress near ϕ_c. We overcome this in two ways. First, we impose a constant shear stress rather than shear rate, which allows the system to flow or not, and the yield stress—the stress below which the material does not flow—can be identified. Second, we impose a constant confining pressure rather than a fixed volume, which allows the system to dilate (or compact)—to change its volume fraction—as necessary under flow. In this way we are able to approach the critical point along trajectories at fixed shear stress and pressure, rather than, as is traditional, along paths of fixed shear rate and volume fraction.

It proves revealing to discuss the behavior from a perspective often used in the granular flow community. Although both the shear and normal stresses diverge at the critical point, their ratio does not. For viscous suspensions the behavior can be described in terms of the friction coefficient μ, a *macroscopic*, effective property of the material, and the viscous flow number I_v [19]

$$\mu = \sigma/\Pi \quad \text{and} \quad I_v = \eta_0 \dot{\gamma}/\Pi, \qquad (1)$$

where σ is the shear stress, Π is the particle (or osmotic) pressure, η_0 is the solvent viscosity, and $\dot{\gamma}$ is the strain rate. Using the viscous flow number I_v—the ratio of an internal suspension time scale η_0/Π to the flow time scale $\dot{\gamma}^{-1}$—Boyer *et al.* [19] successfully unified the rheology of viscous non-Brownian suspensions and inertial-driven granular materials.

For rapid granular flows both the shear and normal stresses scale inertially (as $\sim \rho a^2 \dot{\gamma}^2$) and their ratio, the friction coefficient, is independent of the strain rate, which has led to the claim that a rate-independent friction coefficient is a signature of (dry) friction-dominated material and flow. However, in viscous non-Brownian suspensions (any colloidal suspension at high shear rates) both σ and Π scale linearly with the strain rate (as $\sim \eta_0 \dot{\gamma}$), and the friction coefficient is independent of $\dot{\gamma}$ even though the material behaves as a liquid.

Liquidlike colloidal dispersions are not normally discussed in terms of μ because at low shear rates (strong thermal motion) the shear stress is proportional to $\dot{\gamma}$, but the normal stress is dominated by the equilibrium osmotic pressure and thus $\mu \sim \dot{\gamma}$ as $\dot{\gamma} \to 0$. However, near the flow-arrest point, the material has a dynamic yield stress, and μ may approach a constant as $\dot{\gamma} \to 0$. The friction coefficient perspective therefore enables a natural connection between Brownian suspensions and granular materials.

We study the suspension rheology using Brownian dynamics simulations without hydrodynamic interactions (HIs). In the simulations, we enforce the hard-sphere interactions via the "potential free" algorithm [22–25] and compute ϕ and $\dot{\gamma}$ from the imposed σ and Π, which, when scaled with the thermal energy $k_B T$, give, respectively, the stress Péclet number $Pe_\sigma = 6\pi a^3 \sigma / k_B T$ and the dimensionless pressure $\bar{\Pi} = \Pi a^3 / k_B T$, with a the mean particle radius. The particle dynamics follow the overdamped Langevin equation

$$\zeta\left(\dot{\boldsymbol{x}} - \dot{\gamma} x_2 \boldsymbol{e}_1 - \frac{1}{3}\dot{e}\boldsymbol{x}\right) = \boldsymbol{f}_p + \boldsymbol{f}_b, \qquad (2)$$

where $\boldsymbol{x} = (x_1, x_2, x_3)$ is the particle position in the 1-(velocity), 2-(velocity gradient), and 3-(vorticity) directions, $\zeta = 6\pi\eta_0 a$ is the Stokes resistance, $\dot{e}$ is the expansion rate, $\boldsymbol{e}_1$ is the unit vector in the one-direction, $\boldsymbol{f}_p$ is the interparticle force [25], and $\boldsymbol{f}_b$ is the Brownian force, which has a mean of 0 and a variance of $2k_B T \zeta$. We impose periodic boundary conditions in the 1- and 3-directions and the Lees-Edwards boundary condition in the 2-direction. The strain ($\dot{\gamma}$) and expansion ($\dot{e}$) rates are computed from

$$\sigma = \left(1 + \frac{5}{2}\phi\right)\eta_0 \dot{\gamma} + \sigma_{12}^p, \qquad (3)$$

$$\Pi = -\left(\kappa_0 + \frac{4}{3}\phi\eta_0\right)\dot{e} - \frac{1}{3}\boldsymbol{\sigma}^p : \mathbf{I}, \qquad (4)$$

where κ_0 is the bulk viscosity of the compressible solvent [26] and $\boldsymbol{\sigma}^p = -nk_B T\mathbf{I} - n\langle \boldsymbol{x}\boldsymbol{f}_p\rangle$ is the particle stress contribution, with $n = N/V$ the number density. The simulation box size L is then adjusted isotropically as $\dot{L} = \frac{1}{3}\dot{e}L$. The novelty of our method is that, through a compressible solvent, the constant pressure constraint for the overdamped system is satisfied without introducing permeable boundaries.

For each $(Pe_\sigma, \bar{\Pi})$ pair we perform at least three independent simulations; each contains $N = 200$ particles with 10% particle size polydispersity [8]. The simulation lasts at least 10^4 dimensionless time units with step size 10^{-4}, where the time is scaled with $6\pi\eta_0 a^3 / k_B T$ when $Pe_\sigma < 1$ and with η_0/σ when $Pe_\sigma \geq 1$. In the Supplemental Material [27] we describe the computation of $\boldsymbol{f}_p$ and show
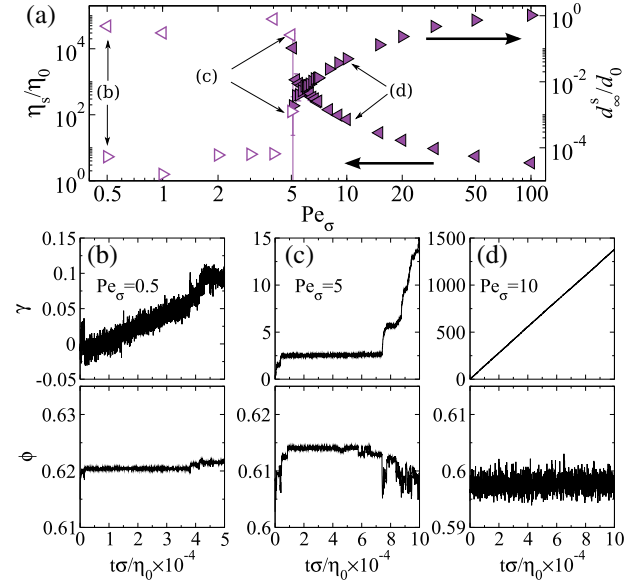

FIG. 1 (color online). (a) The suspension steady shear viscosity η_s/η_0 (left triangles) and the long-time self-diffusivity d_∞^s/d_0 (right triangles), with $d_0 = k_B T/(6\pi\eta_0 a)$, as functions of Pe_σ in constant shear stress and pressure simulations at an imposed pressure $\Pi a^3/k_B T = 5$. The filled (open) symbols represent the flowing (arrested) states. Typical accumulated strain γ (top) and volume fraction ϕ (bottom) at $Pe_\sigma = 0.5$ (b), 5 (c), and 10 (d) as functions of dimensionless time $t\sigma/\eta_0$ are also presented, with the corresponding Pe_σ annotated in (a).

that the selected parameters adequately capture the physics of flow-arrest transitions.

Typical rheological responses from constant stress and pressure simulations at an imposed pressure $\bar{\Pi} = 5$ are shown in Fig. 1. The Pe_σ dependence of the shear viscosity $\eta_s = \sigma/\dot{\gamma}$ and the long-time self-diffusivity d_∞^s, measured from the slope of the mean-square displacement in the vorticity direction $d_\infty^s = \lim_{t\to\infty} \frac{1}{2}d\langle(\Delta x_3)^2\rangle/dt$, are presented in Fig. 1(a). The suspension exhibits a flow-arrest transition at $Pe_\sigma \approx 5$, with the flowing data shown as filled symbols and the arrested data as open symbols. When $Pe_\sigma \gtrsim 5$, the shear viscosity increases sharply with decreasing Pe_σ, reaching $\eta_s/\eta_0 \approx 2 \times 10^4$ at $Pe_\sigma \approx 5$. Accompanying the growth in η_s is an abrupt reduction in d_∞^s. At lower Pe_σ, the shear viscosity remains high and the long-time self-diffusivity low. Figures 1(b)–1(d) show behaviors of the accumulated strain $\gamma = \int_0^t \dot{\gamma}dt$ and the volume fraction ϕ at different Pe_σ. The accumulated strain grows linearly with time in the flowing state but changes little in the arrested state. At $Pe_\sigma = 5$ in Fig. 1(c), γ exhibits instability and switches between the flowing and arrested states. Correspondingly, ϕ fluctuates around a mean value for both the flowing and arrested suspensions but becomes unstable at the flow-arrest point. We found that the suspensions are arrested when $\eta_s/\eta_0 > 2 \times 10^4$ over a wide range of imposed pressures. Consequently, this is adopted as a criterion for the flow-arrest transition in this work.
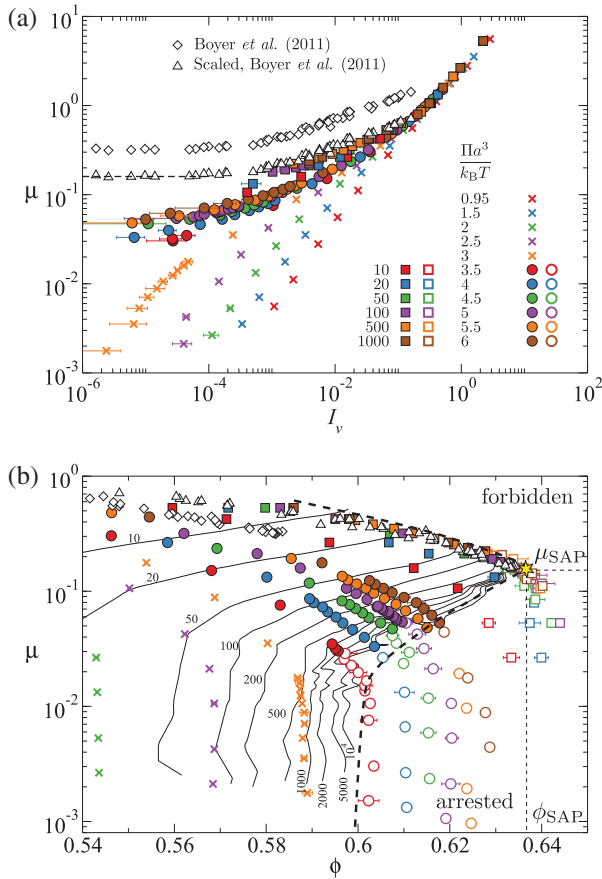
FIG. 2 (color). The steady shear rheology of hard-sphere colloidal suspensions with constant shear stress and pressure. (a) $\mu = \sigma/\Pi$ as a function of $I_v = \eta_0 \dot{\gamma}/\Pi$ and (b) μ as a function of ϕ. Simulations at the same imposed pressure $\Pi a^3/k_B T$ are shown in the same symbols. For suspensions exhibiting flow-arrest transitions, the filled (open) symbols represent the flowing (arrested) states. The raw and the scaled data of Boyer et al. [19] are shown in diamonds and triangles, respectively. In (b), the dashed lines outline the boundary of the flowing region, and the solid lines are contours of the shear viscosity η_s/η_0. The shear arrest point (ϕ_{SAP}, μ_{SAP}) is shown as a star.

Figure 2 presents the overall steady shear rheology at constant stress and pressure near the flow-arrest transition. Figure 2(a) shows the friction coefficient as a function of the viscous number, and Fig. 2(b) shows the corresponding volume fraction. The symbols of the same color are at the same confining pressure (shown in the figure legend) and trace out "isobars." Filled symbols are flowing liquidlike systems, while open symbols denote arrested states.

Starting with solid ×'s at low confining pressures, e.g., at $\bar{\Pi} = 0.95$ in Fig. 2(a), μ grows linearly with I_v at low and high I_v with different slopes; the suspension does not arrest. The ratio of μ and I_v is the shear viscosity $\eta_s/\eta_0 = \mu/I_v$. At high I_v, the suspension viscosity η_s asymptotes to the solvent viscosity η_0. With increasing $\bar{\Pi}$, the μ-I_v curve flattens as I_v decreases but eventually turns down such that $\mu \sim \dot{\gamma}$ as $\dot{\gamma} \to 0$. The suspension flows as a liquid with an increasing zero shear-rate viscosity corresponding to the larger ϕ seen in Fig. 2(b).

When the confining pressure $\bar{\Pi} \geq 3.5$, the suspension arrests and flows only if μ exceeds a limiting value $\mu_m(\bar{\Pi})$, and the minimum shear rate (I_v) increases. The imposed stress corresponding to μ_m is the dynamic yield stress at the imposed pressure. Moreover, μ_m increases with $\bar{\Pi}$ and, as $\bar{\Pi} \to \infty$, μ_m asymptotes to a constant value of 0.16. At high $\bar{\Pi}$ (and high I_v for low $\bar{\Pi}$) all data collapse onto a single curve corresponding to the limiting behavior of non-Brownian viscous suspensions.

Figure 2(b) shows the corresponding μ-ϕ curves. At low confining pressures (the ×'s) the volume fraction increases as the shear stress (μ) decreases. When arrested, $\bar{\Pi} \geq 3.5$ (open symbols), dilation always precedes flow as the shear stress is increased and the maximum flowable volume fraction ϕ_m is always lower than the zero-shear value. As a point of reference, the zero-shear volume fraction at $\bar{\Pi} = 3.5$ is $\phi = 0.60$ for our system. As $\bar{\Pi} \to \infty$, ϕ_m asymptotes to a constant value and the non-Brownian limit emerges as the μ-ϕ curves collapse. The flowing region in Fig. 2(b) is bounded from below by the arrested region and from above by the non-Brownian behavior.

The rightmost point of the flowing region, highlighted as a star in Fig. 2(b), corresponds to the flow-arrest transition in the viscous non-Brownian limit. This point is referred to as the shear arrest point (SAP):

$$(\phi_{SAP}, \mu_{SAP}) = \lim_{\bar{\Pi} \to \infty} (\phi_m, \mu_m) \approx (0.635, 0.16), \quad (5)$$

which represents a limit beyond which the suspension is unable to flow regardless of the imposed pressure and shear stress. The SAP is uniquely determined from the constant stress and pressure rheology protocol and therefore may differ from other "jamming" points [5,6]. In fact, ϕ_{SAP} is lower than the maximum random jammed (MRJ) density of the corresponding polydisperse packing $\phi_{MRJ} \approx 0.645$.

Also presented in Fig. 2(b) are the shear viscosity contours up to $\eta_s/\eta_0 = 10^4$. Horizontal traversal near $\mu = 0$ recovers the equilibrium suspension behavior near the glass transition. The viscosity diverges at $\phi_g \approx 0.6$, which is also found experimentally in similar systems [16,17,30]. Vertical crossing corresponds to the constant volume rheology, and the viscosity exhibits shear thinning. Near the SAP, the range of μ in the flowing region reduces drastically for constant volume rheology. On the other hand, constant stress and pressure rheology allows the suspension to dilate and to find the SAP dynamically, a key merit of our approach.

In the flowing region near the flow-arrest transition both the shear viscosity η_s and the incremental normal viscosity η_n diverge as shown in Fig. 3. The incremental normal viscosity η_n characterizes the flow contribution to the osmotic pressure
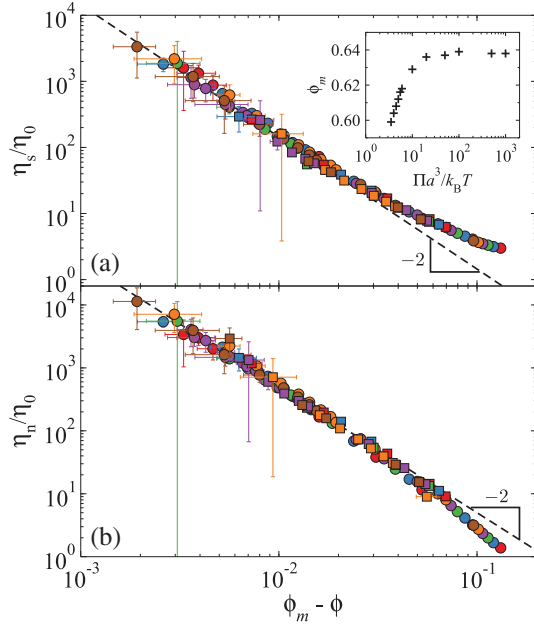
FIG. 3 (color).   Universal viscosity divergences. (a) The shear viscosity η_s/η_0 and (b) the incremental normal viscosity η_n/η_0 as functions of $(\phi_m - \phi)$, the volume fraction difference from arrest, for flowing suspensions with $\bar{\Pi} \geq 3.5$. The inset of (a) shows ϕ_m as a function of $\bar{\Pi}$. The legends are identical to those in Fig. 2.

$$\eta_n = (\Pi - \Pi^{eq})/\dot{\gamma}, \qquad (6)$$

where Π^{eq} is the zero-shear equilibrium osmotic pressure at the same volume fraction. Both η_s and η_n diverge algebraically when approaching the flow-arrest transition: $(\eta_s, \eta_n) \sim (\phi_m - \phi)^{-2}$; the exponent 2 is independent of the imposed pressure and thus valid for both strong and weak thermal fluctuations. The same viscosity divergence exponents were found in experiments [19] and simulations [31] of non-Brownian systems, suggesting the physics of jamming is the most important and universal aspect of the flow-arrest transition. Thermal fluctuations only affect the arrest volume fraction ϕ_m, as shown in the inset of Fig. 3(a).

Note that the divergence of the shear viscosity with an exponent of 2 is not inconsistent with exponent 2.2–2.6 reported for the colloidal glass transition. For the glass transition, one approaches the arrested region in Fig. 2(b) horizontally by varying the volume fraction at low μ, whereas the divergences observed here are for approaching arrest at fixed pressure. Both where the viscosity starts to diverge, ϕ_m, and how steep is the rise, the exponent α, depend on how the "mountain" (the viscosity contours) is approached.

The data collapse in Fig. 3 can be explained by the internal structural relaxations in colloidal dispersions. The inherent relaxation from thermal fluctuations is characterized by $d_\infty^{s,0} = \lim_{Pe_\sigma \to 0} d_\infty^s$, and for glassy materials $\phi > \phi_g$, $d_\infty^{s,0} \to 0$. Comparing the shear to the inherent Brownian forces defines a zero-shear Péclet number $\dot{\gamma}a^2/d_\infty^{s,0}$ and

shows that, in the glassy or arrested state, any finite shear rate gives a *large* Péclet number. The system is driven far from equilibrium and therefore shows universal behaviors. Indeed, this is seen in η_n: linear response would dictate that $\eta_n \propto \dot{\gamma}$ as $\dot{\gamma} \to 0$ [32], rather than be independent of $\dot{\gamma}$ as seen in Fig. 3(b). There is no linear response regime near a flow-arrest point. This may explain why the inherently nonequilibrium isobaric flow-arrest transition of colloidal dispersions has features in common with the athermal granular jamming transitions [33–35].

Finally, we compare our simulations to the experiments of Boyer *et al.* [19], whose results are shown as diamonds in Fig. 2. The experimental data qualitatively agree with the simulation results in the non-Brownian limit ($\bar{\Pi} \to \infty$); however, their flow-arrest critical point $(\phi_c, \mu_c) = (0.585, 0.32)$ is quite different. We can achieve quantitative agreement by scaling the experimental data from (ϕ, μ) to (ϕ', μ') as

$$\frac{\mu'}{\mu} = \frac{\phi_{SAP} - \phi'}{\phi_c - \phi} = \frac{\mu_{SAP}}{\mu_c}, \qquad (7)$$

which are shown as triangles in Fig. 2 and match the simulation results. The scaling of Eq. (7) implies that the fundamental physics behind the viscous non-Brownian arrest does not change with the HIs or the possible frictional contact forces in the experiments. Our simulations clearly capture the physics of the flow-arrest transition.

That $\mu_c > \mu_{SAP}$ can be understood from the lack of HIs in the simulations. Hydrodynamics give an additional contribution to the shear stress via the high-frequency dynamic viscosity, which increases σ and therefore μ. However, they do not explain the difference in the computational ϕ_{SAP} and the experimental ϕ_c seen in Fig. 2(b). One interpretation is that frictional contact forces in the experiments reduce the arrest volume fraction [5,12]. Yet, there is a simpler explanation. In the experiments near suspension arrest, the minimum suspension height in the shear cell (8.8 mm) is not much larger than the particle diameter (1.1 mm) [19,36]. There is a region of order the particle size a adjacent to the apparatus walls that is inaccessible to the particles. Using the accessible volume rather than the total volume can increase the volume fraction by as much as 11% and account for the difference between ϕ_{SAP} and ϕ_c. Clearly, extreme care is needed when studying dense suspensions as seemingly unimportant details can drastically affect the results.

This work demonstrates that constant stress and pressure rheology is an effective approach to study the flow-arrest transitions of dense amorphous materials and provides a unique perspective to distinguish the most fundamental physics in this transition. We found the viscous non-Brownian SAP of hard-sphere colloidal suspensions from the collapse of the flow curves. The results strongly suggest that the jamming and glass transitions are different facets of

the same phenomenon, offering the hope for a unified understanding.

------

*mwwang@caltech.edu
†jfbrady@caltech.edu

[1] N. J. Wagner and J. F. Brady, Phys. Today **62**, No. 10, 27 (2009).

[2] J. F. Morris and F. Boulay, J. Rheol. **43**, 1213 (1999).

[3] F. Varnik, L. Bocquet, J.-L. Barrat, and L. Berthier, Phys. Rev. Lett. **90**, 095702 (2003).

[4] A. J. Liu and S. R. Nagel, Nature (London) **396**, 21 (1998).

[5] D. Bi, J. Zhang, B. Chakraborty, and R. P. Behringer, Nature (London) **480**, 355 (2011).

[6] T. K. Haxton, M. Schmiedeberg, and A. J. Liu, Phys. Rev. E **83**, 031503 (2011).

[7] A. Ikeda, L. Berthier, and P. Sollich, Phys. Rev. Lett. **109**, 018301 (2012).

[8] N. Koumakis, M. Laurati, S. U. Egelhaaf, J. F. Brady, and G. Petekidis, Phys. Rev. Lett. **108**, 098303 (2012).

[9] A. Ikeda, L. Berthier, and P. Sollich, Soft Matter **9**, 7669 (2013).

[10] P. Olsson and S. Teitel, Phys. Rev. E **88**, 010301(R) (2013).

[11] N. Estrada, E. Aźema, F. Radjai, and A. Taboada, Phys. Rev. E **84**, 011306 (2011).

[12] R. Seto, R. Mari, J. F. Morris, and M. M. Denn, Phys. Rev. Lett. **111**, 218301 (2013).

[13] R. Mari, R. Seto, J. F. Morris, and M. M. Denn, arXiv:1508.01243.

[14] C. Heussinger, Phys. Rev. E **88**, 050201(R) (2013).

[15] W. van Megen, T. C. Mortensen, S. R. Williams, and J. Müller, Phys. Rev. E **58**, 6073 (1998).

[16] G. Brambilla, D. El Masri, M. Pierno, L. Berthier, L. Cipelletti, G. Petekidis, and A. B. Schofield, Phys. Rev. Lett. **102**, 085703 (2009).

[17] J. Reinhardt, F. Weysser, and M. Fuchs, Phys. Rev. Lett. **105**, 199604 (2010).

[18] W. B. Russel, N. J. Wagner, and J. Mewis, J. Rheol. **57**, 1555 (2013).

[19] F. Boyer, E. Guazzelli, and O. Pouliquen, Phys. Rev. Lett. **107**, 188301 (2011).

[20] W. C. K. Poon, E. R. Weeks, and C. P. Royall, Soft Matter **8**, 21 (2012).

[21] P. Chaudhuri, L. Berthier, and S. Sastry, Phys. Rev. Lett. **104**, 165701 (2010).

[22] D. M. Heyes and J. R. Melrose, J. Non-Newtonian Fluid Mech. **46**, 1 (1993).

[23] W. Schaertl and H. Sillescu, J. Stat. Phys. **74**, 687 (1994).

[24] P. Strating, Phys. Rev. E **59**, 2175 (1999).

[25] D. R. Foss and J. F. Brady, J. Rheol. **44**, 629 (2000).

[26] Treating the solvent as a compressible fluid allows the periodic unit cell to be expanded isotropically without violating the physics of Brownian particles in Stokes flow; see J. F. Brady, A. S. Khair, and M. Swaroop, J. Fluid Mech. **554**, 109 (2006). Thus, a physical permeable boundary, which can cause local ordering, etc., is not necessary.

[27] See Supplemental Material at http://link.aps.org/supplemental/10.1103/PhysRevLett.115.158301, which includes Refs. [28,29], for algorithm description, simulation validation, and visualization.

[28] C. Toninelli, M. Wyart, L. Berthier, G. Biroli, and J.-P. Bouchaud, Phys. Rev. E **71**, 041505 (2005).

[29] B. D. Lubachevsky and F. H. Stillinger, J. Stat. Phys. **60**, 561 (1990).

[30] D. El Masri, G. Brambilla, M. Pierno, G. Petekidis, A. B. Schofield, L. Berthier, and L. Cipelletti, J. Stat. Mech. Theor. Exp. **2009**, P07015 (2009).

[31] M. Trulsson, B. Andreotti, and P. Claudin, Phys. Rev. Lett. **109**, 118305 (2012).

[32] J. F. Brady and M. Vicic, J. Rheol. **39**, 545 (1995).

[33] E. Lerner, G. Düring, and M. Wyart, Proc. Natl. Acad. Sci. U.S.A. **109**, 4798 (2012).

[34] M. Bouzid, M. Trulsson, P. Claudin, E. Clément, and B. Andreotti, Phys. Rev. Lett. **111**, 238301 (2013).

[35] B. Andreotti, J.-L. Barrat, and C. Heussinger, Phys. Rev. Lett. **109**, 105901 (2012).

[36] F. Boyer, Ph.D. thesis, Aix-Marseille Université, 2011.